Development of Mathematical Model and Characterization of Internal Surface Obtained by Elasto-Abrasives Magneto-Spiral Finishing (EAMSF)

Shivam Yadav
Clemson University, shivamy@clemson.edu

Amit Sangoi
Technological University, absangoi@dbatu.ac.in

Raju Pawade
Technological University, rspawade@dbatu.ac.in

Follow this and additional works at: https://tigerprints.clemson.edu/oa_fund

Development of Mathematical Model and Characterization of Internal Surface Obtained by Elasto-Abrasives Magneto-Spiral Finishing (EAMSF)

Shivam Yadav[1]
Department of Mechanical Engineering,
Clemson University,
Clemson, SC 29631
e-mail: shivamy@clemson.edu

Amit Sangoi
Department of Mechanical Engineering,
Dr. Babasaheb Ambedkar
Technological University,
Lonere, Raigad, Maharashtra 402103, India
e-mail: absangoi@dbatu.ac.in

Raju Pawade
Department of Mechanical Engineering,
Dr. Babasaheb Ambedkar
Technological University,
Lonere, Raigad, Maharashtra 402103, India
e-mail: rspawade@dbatu.ac.in

The implantation of stents and instruments with capillary action demands super-finished internal surfaces of the manufactured product. Elasto-abrasives magneto-spiral finishing (EAMSF) is the attempt made in this paper to enhance finishing productivity by incorporating the abrasive flow in spiral motion due to the presence of the magnetic field. Here, novel impregnated elasto-magnetic abrasive particles (IMPs) are used in a magnetic field-assisted environment to polish the inner walls of the workpiece. In EAMSF, magnetic force provides excess finishing pressure to the abrasives. In contrast, the high-impact polystyrene (HIPS) elasticity absorbs the extra force of the IMPs on the finishing surface. An Indigenous mathematical relation considering the physics of this superfinishing process indicating material removal shows a close resemblance to the experimental results with an error percentage of 1.03 has been developed. The results of the experimentation reveal that 50% concentration of abrasives and a magnetic field density of 18mT yield a superior surface finish with a R_a value equal to 0.053 μm and maximum material removal of 6.9 mg, while in the absence of a magnetic field, excellent surface finish with a $R_a = 0.266$ μm and maximum material removal of 5.4 mg is achieved. In the presence of magnetic field density, significant enhancement of material removal, surface finish, and burr removal is observed. Finishing the surface at 50% abrasive concentration with a magnetic field represents regular finishing, and the trench marks on the original surface are removed after finishing. [DOI: 10.1115/1.4054936]

Keywords: superfinishing, stainless steel 316, high-impact polystyrene, elasto-abrasives magneto-spiral finishing, impregnated elasto-magnetic abrasive particles, grinding and abrasive processes, micro- and nano-machining and processing, modeling and simulation, nontraditional manufacturing processes, powder processing, process engineering, process planning, tribology in manufacturing

1 Introduction

Typical manufacturing processes for producing a part are forging, machining, casting, and forming, while finishing is the concluding operation. Generally, the finishing costs of the workpiece are about 10–15% of the overall cost of manufacturing. Manufacturing exclusively delicate intricate parts demands a peculiar surface texture to retain lubricants. At times the finished surface texture possesses importance for aesthetics. The surface produced due to primary manufacturing processes has inherent features that will not serve the intended use. Hence, there is a need to improve surface characteristics.

The main objective of the present study is surface finish improvement. All conventional finishing processes possess an upper bar of the shape and dimension of the workpiece. The primitive honing methodology is generally employed on cylindrical surfaces whereas, for flat surfaces, lapping is preferred more. The traditional processes also defy in-process control; hence, it is difficult to control the output during the finishing process. A considerable amount of heat is generated and its concentration while the grinding primes on the surface and sub-surface defects in the workpiece. There is a dire necessity to develop a post-manufacturing method

that provides superior surface finish compared to the inevitable conventional finishing methods, whose output parameters can be controlled externally. In contrast, the finishing is in-process and can finish complex shapes and topologically optimized structures with internal cavities [1–4].

The process of using a high-speed rotating screw rod to achieve a fine surface finish of a workpiece is described in the spiral polishing mechanism [3,5–8]. The resharpening of the abrasives takes place during the process of pressing and squeezing. The drill-bit's spiral motion recirculates the abrasives settled at the bottom. During the process, the slurry was allowed to be recirculated for recycling and reusing to reduce the consumption of slurry, thereby reducing polishing expenses efficiently cleaning metamorphic layers and burrs [5–8].

In the spiral mechanism of polishing, abrasive intermixing relies on medium self-deformability and the pressure from the drill-bit. Three flow types can be observed in the finishing zone and where medium remixing occurs after the working region. Diverse arrays of different flows cause the contact between the abrasives and the workpiece surface to be curved to increase the number of contours capable of shear, causing more significant material removal.

1.1 Elasto-Abrasives Magneto-Spiral Finishing Process.
The main idea emphasized in this research is the application of impregnated elasto-magnetic abrasive particles (IMP) instead of commonly used silicon carbide or aluminum oxide pebbles. A
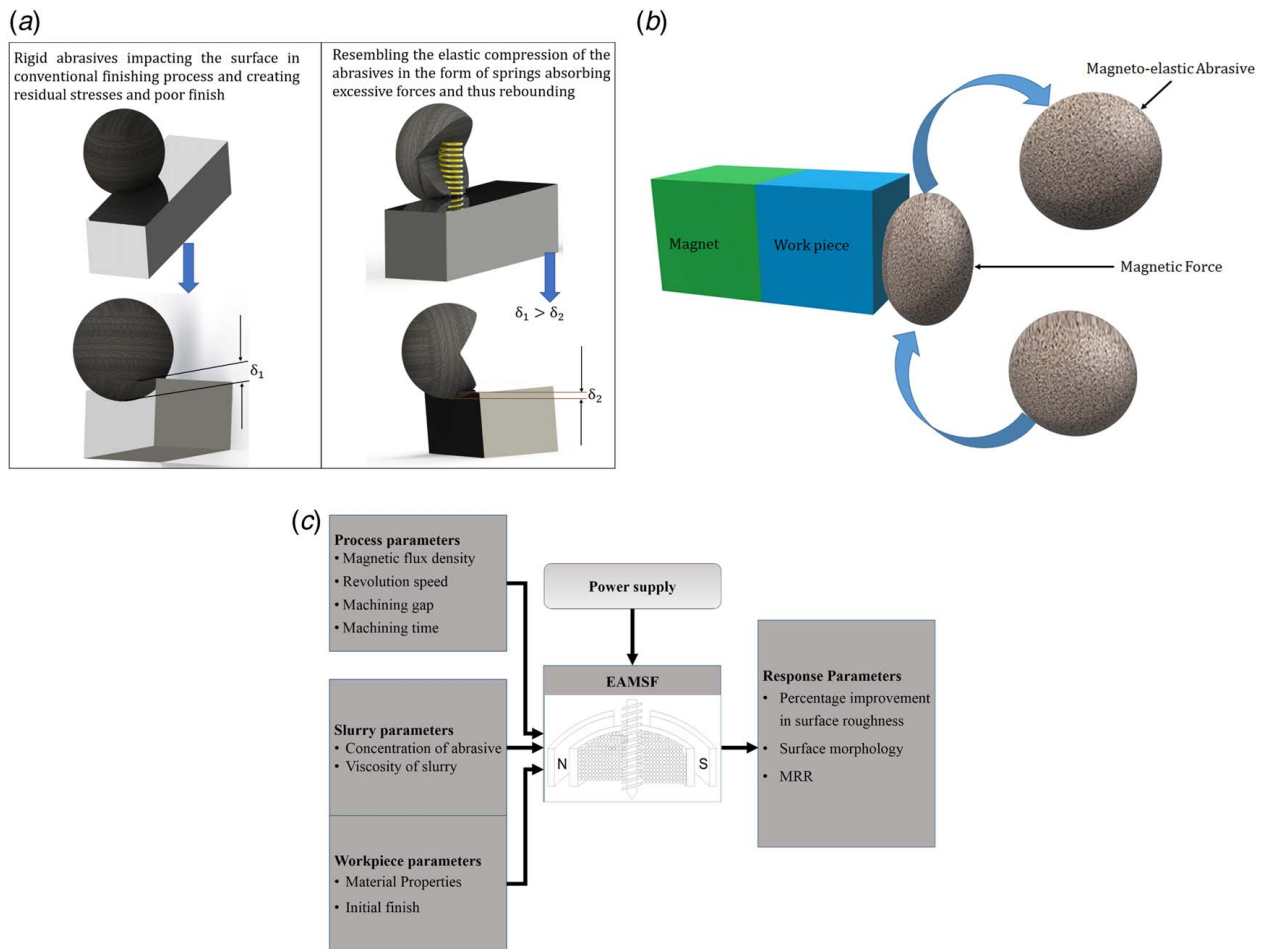
Fig. 1 Overview of the experimental mechanism: (*a*) principle and action of IMP, (*b*) polishing mechanism of IMP, and (*c*) block diagram of EAMSF with different parameters
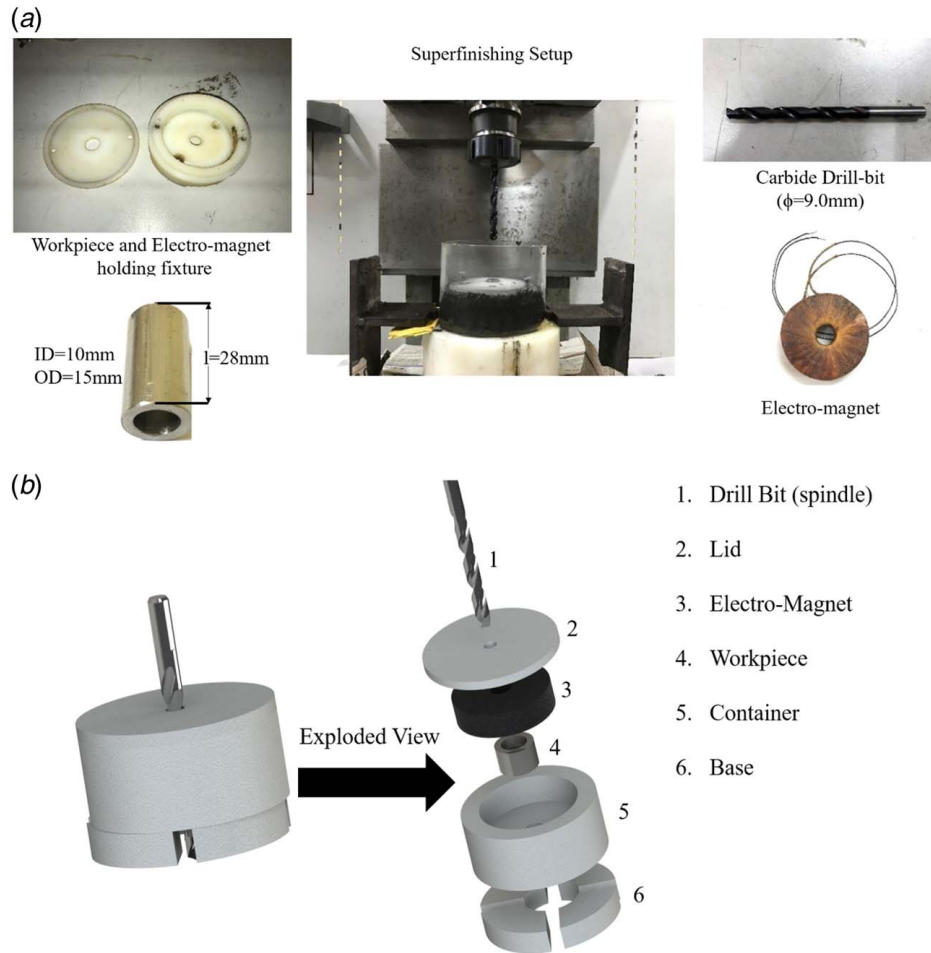
high resistant elastomeric polymer bead with relatively large thermal, chemical, and mechanical stability is used to produce IMP. Resilience is a critical mechanical property when selecting the elastomer for a required application. Elastomeric polymers are marked by high resilience and low Young's modulus [9–12].

As the elastomeric medium exhibit resilient nature, the particles projected to target the surface for erosion behaved like a spring-mass system. Figure 1(*a*) denotes the effect of an IMP along with its spring-mass equivalence. Ideally, the energy consumed for the erosion can be approximated to the change in kinetic energy during the impact [13,14]. For conventional abrasives, a negligible amount of energy is absorbed and recovered by them. However, the IMPs have elastic high-impact polystyrene (HIPS) as the base material over which the abrasive particles are embedded, providing significant loss in the energy on impact and recovery of the energy lost during the rebound of the IMPs. Here, the energy exchange for erosion is relatively lower than the conventional abrasives due to the elastic impact of the IMPs on the workpiece surface. As a result, for the same impact velocity, mass, and size, the erosion depth is lower in elastic abrasives (δ_1) than a conventional abrasive grit (δ_2).

In the elasto-abrasives magneto-spiral finishing (EAMSF) process, IMP would flow easily by rapid turning rod, as the slurry has high fluidity. As the slurry surges through the surface of the workpiece, IMPs are rushed toward the circumferential magnet, which constantly presses and squeezes the work surface, ultimately getting fine polishing. The turning rod directs the abrasives upward, polishing the workpiece's surface [6,12].

The IMP predominantly served two purposes, as depicted in Fig. 1(*b*). Improvement in polishing effect by applying the magnetic

force and getting the cushioning effect done [6,15–18]. The magnetic force developed by the external magnet added a surplus effect to the machining during the flow and impact of the abrasives. The collective outcome of the polishing quality and the influence of magnetic force significantly reduces the machining time [15,17,19]. A rotating rod is introduced into the flowing abrasive medium to enhance the finishing rate using centrifugal force [19–22]. Here, a rise in self-deformability of the medium obtained positive results improving material reduction and the rate of finishing process [23–27]. Investigators also tried placing a rotating drill-bit at the epicenter of the workpiece [7,14,22]. Numerous flow losses occurred amongst the workpiece and tooling, which lowers the probability of dynamic abrasive grain–workpiece contact. Some researchers tested the rotating workpiece in the abrasive flow finishing (AFF) technique [27,28]. The inception of a magnetic field along the workpiece with magnetic abrasives considerably enhanced surface finish and material removal rate [28]. Figure 1(*c*) depicts a chart of magneto-spiral finishing. By varying the rotational speed of the drill-bit, which acts as a screw for lifting the IMPs, superficial finishing improves at 1000 rpm; the abrasive particles roughen the surface heavily at a higher revolutionary pace than the drill-bit. Analogous trends are also cited [29,30] for various rotational speeds of the Custom Fly Grip (CFG) rod. ΔR_a improves with the rise in the revolution speed of the CFG rod. The drawbacks of the conventional finishing processes are primarily its inability to finish complex geometries and the technique being limited by the shape and dimensions of the workpiece [31–33]. These processes also lack in-process control, due to which the final finish of the workpiece does not meet the expectations of superiority. During grinding, large quantities of

(a)

Superfinishing Setup

Workpiece and Electro-magnet
holding fixture

ID=10mm
OD=15mm

l=28mm

Carbide Drill-bit
(φ=9.0mm)

Electro-magnet

(b)

Exploded View

1. Drill Bit (spindle)

2. Lid

3. Electro-Magnet

4. Workpiece

5. Container

6. Base

Fig. 2 Representation of the actual and modelled experimental setup: (a) experimental apparatus along with dimensional details of the actual workpiece and (b) schematic and exploded view of the experimental setup

intense heat are generated, resulting in surface and sub-surface defects in the workpiece [29,30,34,35].

2 Experimental Work

As illustrated in Fig. 2, the workpiece material is SS316 seamless pipe of ID 10 mm and OD 15 mm. For ease in experimentation, the whole piece of tube is cut into smaller pieces of the length of 28 mm. The previous inner surface roughness was $R_a = 3.236\ \mu m$, $R_q = 6.03\ \mu m$, and $R_z = 3.76\ \mu m$. The magnetic field application was discharged alongside slurry concentration variation in the first set of experiments. Later in the second set of experiments, spiral finishing was performed without applying a magnetic field.

EAMSF used a rotating drill-bit to drive the slurry up from the cylindrical workpiece. The flow of slurry consisting of IMPs is not constant in the setup. Due to the viscous nature of IMP, it takes time for slurry to reach the bottom from the top and recirculate again. Increasing the drill-bit diameter increases the material removal rate from the target surface due to the high pressure on abrasives. Due to this, a cross section for the flow of abrasive results in high indentation depth, consequently resulting in a high material removal rate. A drill-bit was carefully centered to the specimen, and coordinates were fed into the machine. Drill-bit is the driver as it guides the IMPs in flutes and drives up from the workpiece, finishing the inner surface in the process. Drill-bit is used to flow and circulate the abrasive laden medium around the finishing surface in a spiral direction. Flutes of drill-bit lift the slurry upward during rotation. The drill-bit used in experiments is a solid carbide drill-bit of diameter 9.0 mm. The clearance between the drill-bit and workpiece, also called the machining gap, is 0.5 mm. The magnetic field was switched ON only when there was a flow. The current through the magnet was kept constant at 1A throughout the experiment. Next, the experiments were conducted in the absence of a magnetic field. Composite abrasives were used to perform these experiments IMPs without embedding the Fe3O4 particles. The quantity of silicon oil was changed to account for the setup volume.

2.1 Analysis of Impregnated Elasto-magnetic Abrasive Particle.
The substrate for the abrasives was selected as an elastic polymer called HIPS. The properties of HIPS are given in Table 1. A temperature above the thermal deformation temperature of 105 °C was provided to the silicon carbide (SiC) particles. Then, the heated SiC particles were allowed to interact and melt the surface of HIPS. The heat contained in the SiC particles

Table 1 Properties of HIPS

Izod impact (notched) (J/m)	Specific gravity	Flexural strength (MPa)	Elongation (at break)	Softening point (°C)	Tensile strength (MPa)
110	1.03	44	50%	102	28
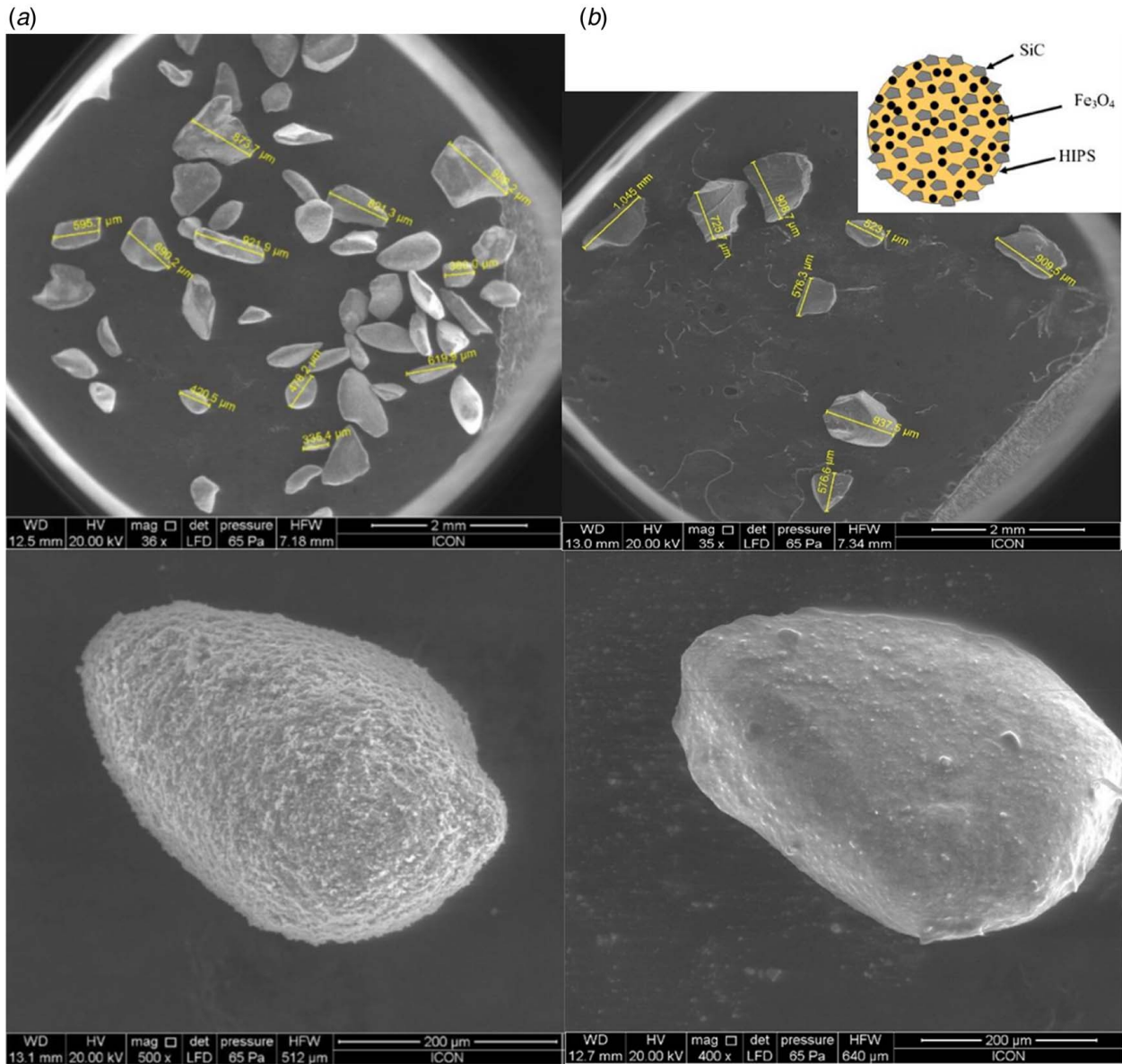
Fig. 3 Study of the abrasives (IMPs) and elastic base material (HIPS): (*a*) Size representation of HIPS, and SEM image of single grain of HIPS, (*b*) size representation of IMP, schematic representation of IMP particle, and SEM image of single grain of IMP particles, (*c*) before EAMSF process, (*d*) during EAMSF process, (*e*) after EAMSF process, and (*f*) SEM image of the slurry

accompanied by vibrations provided to the mixing container was sufficient for them to get embedded on the surface of HIPS and form a uniform coating. Figures 3(*a*) and 3(*b*) illustrate the scanning electron microscope (SEM) photograph of HIPS and IMPs.

In Figs. 3(*c*)–3(*f*), images captured by SEM show the surface of IMP specimens at 5000× zoom level. The following figures show that due to the intergranular fracture mechanism and impinging mechanism during the process, the closely packed sharp grains of the IMPs are slit. And the surface appears to be a lot smoother than the original specimen. However, the base elastomer remains intact in size and shape; hence, the overall size of the IMPs does not vary; only the surface turns smooth.

2.2 Working of the Electromagnet. For experimentation, a ring-type electromagnet was manufactured. The electromagnet's windings resemble a finite solenoid, creating a parallel magnetic field line in the axial direction at the center of the solenoid. The electromagnet's windings resemble a finite solenoid, creating a parallel magnetic field line in the axial direction at the center of the solenoid

as depicted in Fig. S1 (available in the Supplemental Materials on the ASME Digital Collection). The IMPs moving in the magnetic field will be attracted towards the magnet, thus squeezing the IMPs on the workpiece surface due to magnetic force. This impressed pressure and an application of the magnetic field will cause enhanced polishing effects on the workpiece's surface, resulting in improved material removal and polishing efficiency.

Each experiment was conducted for 40 min. Experimentation for EAMSF using IMP, as shown in Fig. 3, is conducted in this study. The scope of the developed system is examined by designing the experiments using a one factor at a time approach. To evaluate the newly developed setup, two sets of experiments were conducted.

3 Mathematical Modeling

The EAMSF process can be easily quantified into a mathematical relationship of material removal mechanism, considering the performance and parameters during the process. The calibration of the
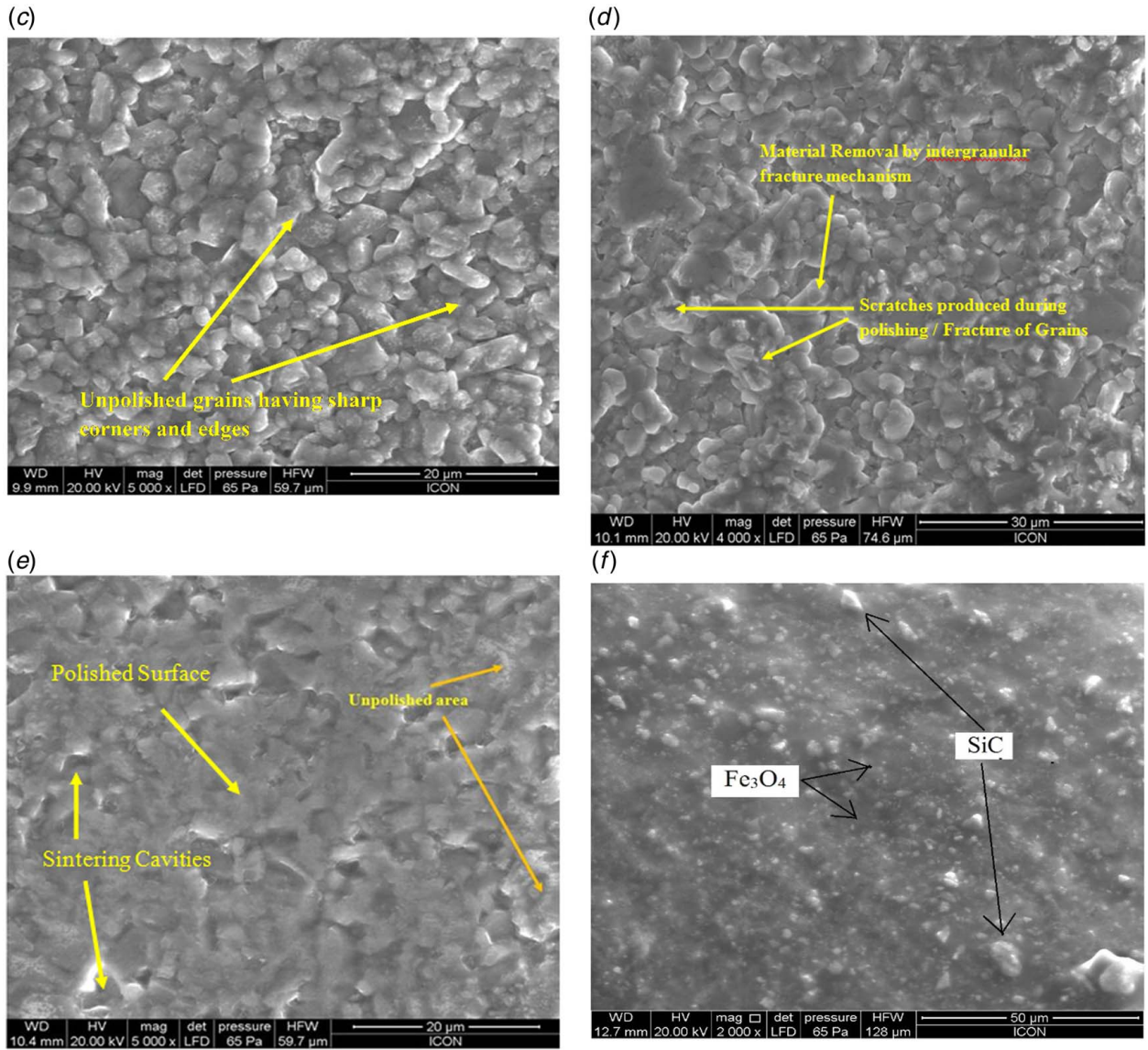
(c)

(d)

(e)

(f)

Fig. 3 Continued

forces acting on the workpiece and the material removal mechanism can be easily understood. In this process, the sintered particles of Fe_3O_4 and SiC are impregnated over high-impact polystyrene (HIPS) balls, as shown in Fig. S2(a) (available in the Supplemental Materials on the ASME Digital Collection), which forms the composition of the IMPs. IMPs initially flow through the grooves of the drill-bit. At the same time, on the application of a magnetic field, they immediately start to flee radially outward, impinging the cylindrical workpiece on the internal wall [12]. Thus, a composite material that is non-linear and possesses irregular geometry is contained in the machining gap. The finite element method is used to obtain the governing equation of the magnetic field to quantify the material removal.

3.1 Governing Equation. The model is developed based on certain assumptions which follow Maxwell's equations.

(1) Magnetic field intensity is constant with time during the EAMSF process [36–39].
(2) As the working gap is a few millimeters, there is no magnetic field leakage.
(3) Magnetic field lines penetrate the workpiece surface, and the IMPs are in the form of clusters and travel radially outward.

(4) As the process is under the superfinishing category with significantly less material removal, which is clear from the experimental results; therefore, the chips do not showcase any substantial effect on the EAMSF process.
(5) As the experiment setup is symmetrical to the cylinder's axis, as shown in Fig. S2(b) (available in the Supplemental Materials on the ASME Digital Collection), the solution's domain is also symmetrical.

The gradient of the scalar magnetic potential (φ) is defined as the magnetic field intensity (H), which is denoted by the following equation [36–39]:

$$H = -\nabla\varphi \tag{1}$$

Based on the above assumptions, in the axis-symmetric form, the governing equation of the process becomes [36–39]

$$\frac{1}{l}\frac{\partial}{\partial l}\left[r\mu_l\frac{\partial\varphi}{\partial l}\right] + \frac{\partial}{\partial r}\left[\mu_l\frac{\partial\varphi}{\partial r}\right] = 0 \tag{2}$$

where φ is the scalar magnetic potential, and μ_l is the relative permeability of IMPs.

While r is the radius of the projected circular area of indentation and l represents the length of the path of the indentation along the workpiece surface.

The variation in the permeability of magnetic particles with the magnetic flux infers the non-linear nature of Eq. (2).

4 Boundary Conditions

The following boundary conditions are established while developing the model. The machining zone under consideration is axisymmetric to the axis of the cylindrical workpiece; hence, only one cut piece is used for analysis to decipher the domain of the solution. The domain of the solution is represented in Fig. 4. The boundary domain consists of a projected rectangular cross-section with four sides: Q_1, Q_2, Q_3, and Q_4.

(1) Critical boundary conditions:
In $Q1$ and $Q3$, the magnetic potential φ is calibrated as zero and product of number of turns and input current in the solenoid (NI), respectively

$$\varphi = 0 \text{ on } Q_1 \tag{3}$$

$$\varphi = NI \text{ on } Q_3 \tag{4}$$

where N is the number of turns and I is the input current in the solenoid.
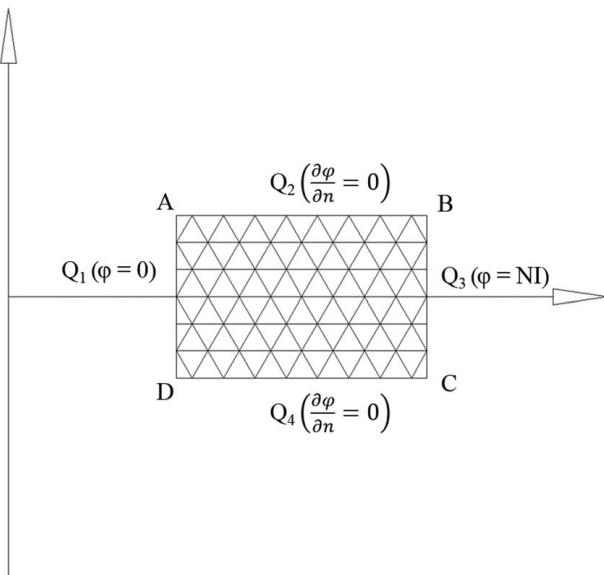
(2) Natural boundary conditions:
At the exterior position, the extreme ends in transverse directions marked by sides Q_2 and Q_4. The magnetic potential derivative normal to it is zero as the equipotential lines lie perpendicular to this boundary.

$$\frac{\partial \varphi}{\partial n} = 0 \tag{5}$$

5 Finite Element Analysis

Galerkin's finite element method is used for evaluating the potential magnetic distribution in the solution domain [36–39]. Quadrilateral elements with eight nodes are assessed for discretizing the domain, as shown in Fig. 4.

5.1 Equations and Procedure of Solution With the Finite Element. Applying the boundary conditions presented in

Fig. 4 Boundary conditions and finite element meshing of the projected area of the cut section of a cylindrical workpiece

Eqs. (3)–(5) and substituting in Eq. (2), the following expression in algebraic form is obtained [36,37]

$$[K]\{\varphi\} = \{0\} [K]\{\varphi\} = \{0\} \tag{6}$$

where $\{\varphi\}$ is the vector with global magnetic potential, and $[K]$ is the matrix with global coefficient. In the given domain, all the nodes consist of a particular value of the vector φ called the nodal value. The accumulation of matrices composed of the elemental coefficients of all elements results in evaluating the $[K]$. The general form of a matrix with elemental coefficient $[k]^e$ is represented by the following equation:

$$[k]^e = \int_{A_e} \mu_l [\beta]^{eT} [\beta]^e 2\pi dl dz \tag{7}$$

where $[\beta]^e$ is the shape function derivative matrix, and A_e is the domain of area element.

Gauss–Legendre quadrature is used for computing Eq. (7), which consists of three Gauss points in each direction. The magnetic field strength significantly affects the value of μ_l, which depends on the scalar magnetic potential. There is a variation of solutions in consecutive iterations, which is represented as

$$\varepsilon = \frac{\sqrt{\sum_{i=1}^{tnn} |\varphi_i^{(k)} - \varphi_i^{(k-1)}|^2}}{\sqrt{\sum_{i=1}^{tnn} (\varphi_i^{(k-1)})^2}} \tag{8}$$

where tnn is the total number of nodes, and k is the iteration number.

Iterations are done to reach the tolerance value of ε. The boundary conditions are executed on the equations and are solved using the Gauss Elimination Method.

5.2 Calculation of the Resulting Variables. Accurate values of the resulting variables are obtained at Gauss Point. The magnetic field, its intensity, and the magnetic force are calibrated at the Gauss Points [36–39].

The magnetic field strength and the magnetic affinity of the particle define the amount of magnetic force exerted on the particle. The magnetic potential energy ($P.E._m$) of the particle depends on the location of the particle in the magnetic field, which is represented as [36–39]

$$P.E._m = \frac{\mu_0}{2} \int_v \chi_r H.H dv \tag{9}$$

where v is the particle volume, χ_r is the magnetic susceptibility, μ_o is the absolute permeability of IMPs, and H is the magnetic field intensity

Magnetic potential energy gradient is the force (F) exerted on the particle as a result of the magnetic field. The axial and radial components of the force can be stated as

$$F_a = \frac{\mu_0}{2} v \frac{\partial}{\partial r} (\chi_r H.H) \tag{10}$$

$$F_r = \frac{\mu_0}{2} v \frac{\partial}{\partial z} (\chi_r H.H) \tag{11}$$

The composition of the IMPs includes magnetic particles, SiC as abrasives, and HIPS balls as base material. By Wiedemann's law, the overall magnetic susceptibility [36,38,39] can be expressed as

$$\chi_r = a\chi_{rmp} + b\chi_{rSiC} + (1 - a - b)\chi_{rHIPS} \tag{12}$$

where a is the fraction of volume of magnetic particles, b is the fraction of volume of SiC abrasive particles, χ_{rmp} is the susceptibilities of magnetic particles, χ_{rSiC} is the susceptibilities of SiC, and

χ_{rHIPS} is the susceptibility of HIPS (High Impact Polystyrene).
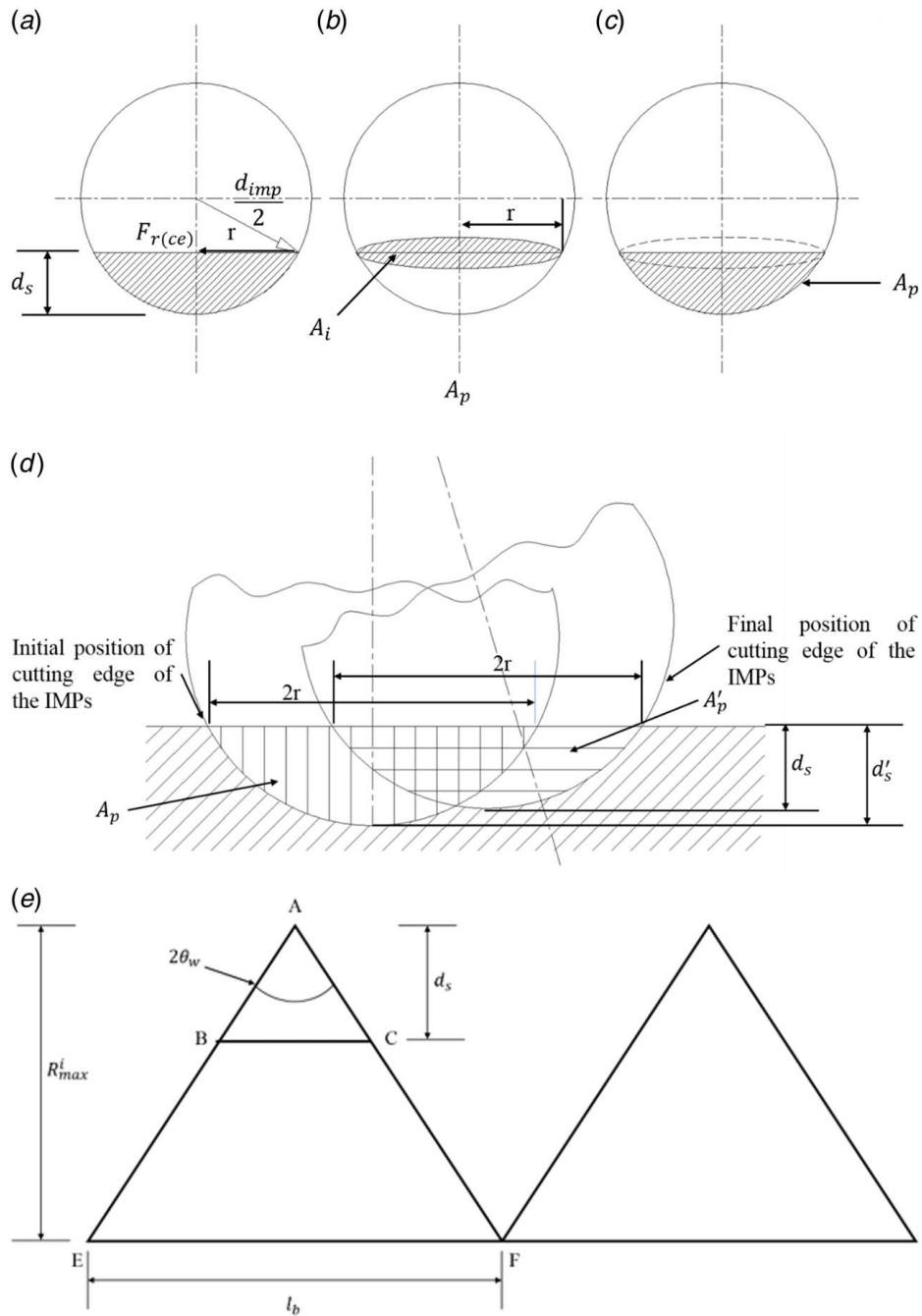
Fig. 5 Schematic view of the abrasive particles penetration: (a) depth of penetration, (b) area projection indicating penetration, (c) penetration area projection, (d) motion indicator of the particle involving actual and apparent depth of penetration, and (e) profile geometry shape of the indentation

The magnetic forces' evaluation occurs at the contact surface between the workpiece and the elements called Gauss points using the correlation between magnetic field intensity and its derivatives. The results are either interpolated or extrapolated to evaluate the forces due to the magnetic field at the actual contacting points. Hence, the determination of the exact location of the point is necessary.

In the experiments, the tool is placed at the central location in the magnetic field while the workpiece is cylindrical in geometry, with the surface being magnetically charged. It is assumed that the IMPs are packed closely in each track and travel along straight lines. The length of the track is defined by the location at which the particles meet the surface. Let us assume the track number as "p" the point of

contact location is given by the equation

$$L_p = (p - 1)D_{imp} + \frac{D_{imp}}{2} \tag{13}$$

where L_p is the length of the pth track and D_{imp} is the diameter of the IMP (presumed to be identical for each IMP). The total number of tracks (n_t) in the array is given by

$$n_t = \frac{\text{Length of the elasto} - \text{Magnetic abrasive array}}{D_{imp}} \tag{14}$$

The length of the IMP array at the interface of the workpiece is equal to the length DC in Fig. 4, and D_{imp} is represented in Fig. 5

5.3 Material Removal Considerations. An array of IMPs is shaped by the application of a magnetic field in the machining gap. The drill-bit's rotation leads to the IMP array's linear flow. The cutting edges of the IMPs are subjected to the development of tangential force (F_t). The energy of the magnetic creates the axial (F_a) and normal (F_r) magnetic forces on the IMPs [20]. The magnetic force in the normal direction (F_r) generates an equal and opposite force on the compressive workpiece surface. Therefore, the workpiece is penetrated by the cutting edge of the IMPs. The cutting edges of the IMPs are subjected to a resultant of the tangential and axial magnetic forces, which leads to the material removal due to the shearing action of the IMPs on the surface of the workpiece along the helical paths, which is assumed to be linear. It can be conveyed that the mechanical power at the spindle tip (drill-bit) in combination with the magnetic force is employed to finish the surface. The force acting tangential to the IMPs is responsible for the material removal from the surface, which is distributed homogeneously. The power induced in the finishing operation is the combination of the multiplication of the cutting speed and cutting-edge tangential force.

The total number of cutting edges $(n_{ce})_p$ in the pth track is given by

$$n_{ce(p)} = \frac{n_a \sqrt{(L_p)^2 + r^2}}{D_{imp}} \tag{15}$$

where n_a is the active number of cutting edges of IMPs (assumed to be 1 in this case).

Cutting speed of a particle in the pth track ($V_{C(p)}$) is given by

$$V_{C(p)} = 2\pi N_s \sqrt{(L_p)^2 + r^2} \tag{16}$$

where N_s is the rotational speed of the spindle. With this, the finishing power can be evaluated as

$$P = \sum_{p=1}^{n_t} F_{t(ce)}(n_{ce(p)} V_{C(p)}) \tag{17}$$

where $F_{t(ce)}$ is the cutting-edge tangential force.

Substituting Eq. (15) containing $n_{ce(p)}$ and Eq. (16) containing $V_{C(p)}$ in Eq. (17), the cutting-edge tangential force is presented as

$$F_{t(ce)} = \frac{P}{\sum_{p}^{n_t} \left(\frac{2\pi(L_p^2 + r^2)N_s n_a}{D_{imp}} \right)} \tag{18}$$

The resultant of the tangential force (F_t) and the axial force (F_a) results in the cutting force (F_c)

$$F_c = \sqrt{F_t^2 + F_a^2} \tag{19}$$

As observed in the flow characteristics of the IMPs, it was observed that the value of the tangential force is quite negligible in the overall effect of the cutting force. The phenomenon can be easily observed in the texture of the surface observed after machining the surface.

Shear strength (τ_s) and the penetration area (A_p) on the surface of the workpiece are resembled by the projection together account for the force (F_{mr}) necessary for the removal of material which is given by the equation

$$F_{mr} = \tau_s A_p \tag{20}$$

In the EAMSF process, while material removal, any of the three given conditions are prevalent. These are the following:

(1) $F_{mr} = F_{c(ce)}$
This indicates the equilibrium condition that reveals that the finishing operation has commenced.
(2) $F_{mr} < F_{c(ce)}$

Material removal occurs in the condition given earlier.
(3) $F_{mr} > F_{c(ce)}$
No material is removed in the condition given above. This equation represents the rotary motion of the IMPs regulates and controls the penetration depth of the cutting edges of the IMPs such that the required force for cutting is in synchronous with available force at the cutting edges keeping all other parameters constant:

$$F'_{mr} = F_{c(ce)} \tag{21}$$

where F'_{mr} is the revised required cutting force.

$$F'_{mr} = \tau_s A'_p \tag{22}$$

where A'_p is the revised projected area of penetration.

Substituting the value of F'_{mr} from Eq. (21) in Eq. (22), we get

$$A'_p = \frac{F_{c(ce)}}{\tau_s} \tag{23}$$

6 Assumptions of the Model

The following assumptions are made for simplifying the computation work to develop the material removal model:

(1) Workpiece surface is assumed to have a uniform surface profile which is triangular shaped.
(2) IMPs do not possess relative motion and are packed closely along the magnetic force lines forming an array. Hence, the porosity between the particles is very low.
(3) The IMPs are assumed to have spherical geometry and uniform size. The shape of IMPs is considered spherical with uniform sizes. It is believed that only one cutting edge is interfering with the workpiece at a time; therefore, material removal takes place only on the track where the edge follows, which is linear. Thus, an equal amount of material is removed from each track.
(4) The compensation of the elastic nature of IMP, which is neglected while deriving the mathematical model, has been made by reducing penetration depth. As the model does not evaluate the workpiece's surface finish, such an assumption can be made.
(5) The gap between the spindle and the workpiece remains constant for all time during the experiment as the material removal is relatively small.

6.1 Material Removal Model. The material removal rate of the workpiece is relatively low in the EAMSF process due to the flowing penetration of the IMPs. The material removal volume can be quantified as the product of the length of the workpiece to be finished and the area of shear on the workpiece.

The force exerted by the IMPs on the surface of the workpiece is directly proportional to the magnetic force acting in the normal direction of the IMPs (F_r) and inversely proportional to the number of active cutting edges encountering the workpiece (n_a). Hence, the magnetic force acting on the IMPs in borders transferred partially depends on the number of active particles responsible for the material removal. The workpiece to be finished is penetrated by a magnetic force acting normal to the workpiece, which is in radially outward direction represented as ($F_{r(ce)}$) given as

$$F_{r(ce)} = \frac{F_r}{n_a} \tag{24}$$

where F_r is the magnetic force acting in the normal direction on the IMP

The number of active edges of the IMPs bombards the surface with a magnitude of force equal to $F_{r(ce)}$ where ΔA is the projected area of indentation, which is microscopic. The hardness is resistant to indentation, which is applied in this case by the force $F_{r(ce)}$.

Hence, the force $F_{r(ce)}$ divided by the projected indentation area is taken as hardness. By equating the reaction force of the IMP on the surface with the force applied, an evaluation of the penetration depth is formulated [37]:

$$F_{r(ce)} = H_m \Delta A \tag{25}$$

where H_m is the workpiece hardness, and ΔA is the indentation projected area (hatched area of Fig. 5(b)).

The hardness considered for the given content explains the equity between the radially outward force and the hardness as the property of a particular workpiece material (hence the reaction force may vary depending upon the property of the used workpiece material). Let r be the radius of the circular indentation projected area. The equation for r is formed as

$$r = \sqrt{\frac{F_{r(ce)}}{\pi H_m}} \tag{26}$$

As seen in Fig. 5(a), penetration depth (d_s) is represented as

$$d_s \leq \frac{d_{imp}}{2} - \sqrt{\left(\frac{d_{imp}}{2}\right)^2 - r^2} \tag{27}$$

where d_{imp} = IMP diameter. Substituting the value of "r" from Eq. (27), we get

$$d_s \leq \frac{d_{imp}}{2} - \sqrt{\left(\frac{d_{imp}}{2}\right)^2 - \frac{F_{r(ce)}}{\pi H_m}} \tag{28}$$

The projected area of penetration is represented as the shaded area in Fig. 5(c), and the depth of penetration (d_s) is indicated in Fig. 5(a), which is exposed to shear force in the EAMSF as obtained from the geometry

$$A_p = \left(\frac{d_{imp}}{2}\right)^2 \left[\cos^{-1}\left(1 - \frac{2d_s}{d_{imp}}\right)\right] - \left[\left(\frac{d_{imp}}{2} - d_s\right)\sqrt{d_s(d_{imp} - d_s)}\right] \tag{29}$$

Fig. S3 (available in the Supplemental Materials on the ASME Digital Collection) diagrammatically depicts that the IMPs travel along the surface of the workpiece in a circular direction. Therefore, the material removal mechanism also occurs in the circular path along the cutting edges of the IMPs, which is represented in Fig. S3 (available in the Supplemental Materials on the ASME Digital Collection). After completing one revolution, the IMPs move in the axial direction in steps completing a revolution at each step. Division of the surface of the workpiece into unit square cells simplifies the evaluation of surface roughness and material removed. The center of the cell is chosen to be the origin, and the coordinates are specified relative to the center. The material removal occurs along the track of the IMPs, which pass through each cell. Material removal calculations are done by the following method.

Let R is the original surface roughness of the surface

The IMPs remove a specified amount of material from each cell (i, j) in the nth revolution, which is given by

$$\Delta V_{ce(i,j)}^{(n)} = A_{p(p)} l_{t(i,j)}^{(n)} \tag{30}$$

where $A_{p(p)}$ = pth track shear area as discussed earlier $l_{t(i,j)}^n$ is the total contact length of the IMPs in the nth revolution of the cell (i, j) along the surface

The contact length of the IMP in cell (i, j) can be defined as the multiplication of the contact length of a single profile $l_{(i,j)}^n$ and the number of profiles (n_f) in the cell (i, j)

$$l_{t(i,j)}^{(n)} = n_p l_{(i,j)}^{(n)} \tag{31}$$

From Fig. 5(e), for a single profile, BC is the contact length which can be evaluated as

$$l_{(i,j)}^{(n)} = 2d_{sp}^n \tan \theta_w \tag{32}$$

where d_{sp}^n is the penetration depth achieved by the IMPs in the track number p, $2\theta_w$ surface profile mean angle.

The manufacturing process and the original roughness of the surface govern the surface profile mean angle. Figure 5 indicates the surface of the workpiece split up into several cells. An enlarged cell is demonstrated in Fig. 5(d). The IMPs shear off the peaks in the profile in the direction normal to the direction of its position. From Fig. 5, we evaluate

$$n_p = \frac{l_c}{l_b} \tag{33}$$

where l_c is the cell length and l_b is the length of the base in a particular profile.

From Fig. 5(e), l_b is given by

$$l_b = 2R_{max}^i \tan \theta_w \tag{34}$$

Substituting Eqs. (31)–(34) into (30), we get

$$\Delta V_{ce(i,j)}^{(n)} = \frac{A_{p(p)} d_{sp}^n l_c}{R_{max}^i} \tag{35}$$

The total volume of material removed in a cell (i, j) in the nth revolution is

$$\Delta V_{(i,j)}^{(n)} = \Delta V_{ce(i,j)}^n n_{ce(p)} \tag{36}$$

Substituting the value of $\Delta V^{(n)}$ from Eq. (35) and $n_{ce(p)}$ from Eq. (15) in Eq. (36)

$$\Delta V_{(i,j)}^{(n)} = \frac{A_{p(p)} d_{sp}^n l_c n_a \sqrt{(L_p)^2 + r^2}}{D_{imp} R_{max}^i} \tag{37}$$

To compute the cumulative volume of material removed in a particular cycle, the summation of the volume of removed material from each cell should be done, which is given as follows for an nth rotation

$$\Delta V^{(n)} = \sum \Delta V_{(i,j)}^{(n)} \tag{38}$$

However, this model applies only when all the abrasive particles are in contact with the surface, and every portion of the workpiece is uniformly finished. As a result of this, this can only occur when the concentration of the slurry is more than 50% concentration.

7 Results and Discussion

The experimental details are given in Table 2.

7.1 Effect of Abrasive Concentration. Figures 6(a) and 6(b) represent the effect of abrasive concentration on surface roughness with and without the presence of magnetic field density. The graph shows that as the slurry concentration increases, the surface finish improves, especially at the concentration of 50%. With increasing concentration, the chances of the workpiece and abrasive interaction also increase as oil content decreases from 60% to 50%, and abrasive starts to abrade the surface instead of sliding over it. The results of material removal also support this behavior. The effect of increasing concentration is significant on material removal.

However, further increasing abrasive concentration, the surface finish starts to worsen because if more abrasive is added to the slurry, the fluidity of the slurry primarily results in a reduced flowrate, which was evident at the time of the experiment. Due to this, overall interaction between workpiece and abrasive decreases resulting in less finish and lower material removal.

7.2 Effect of Magnetic Field. Figure 6(c) compares the effect of variable concentration of slurry on surface roughness with and

Table 2 Experimental results

Sl. N.	Magnetic flux density (with/without) (milli-Tesla)	Slurry concentration (%)			Surface roughness (μm)				Material removal (mg)
		Weight of Si oil(g)	Weight of abrasive (g)	%	R_a (μm)	R_q (μm)	R_z (μm)	R_k (μm)	
1.	18 mT	80	32.8	40	0.0905	0.115	0.663	0.552	6.2
2.	18 mT	80	40	50	0.0535	0.103	0.827	0.242	6.9
3.	18 mT	80	30.2	60	0.0828	0.104	0.401	0.249	5.4
4.	18 mT	80	56	70	0.0912	0.118	0.811	0.560	4.3
5.	Zero	90	36	40	0.309	0.498	3.802	0.589	4.6
6.	Zero	90	45	50	0.266	0.417	3.029	0.6	5.4
7.	Zero	80	48	60	0.297	0.494	3.255	0.597	3.6
8.	Zero	80	56	70	0.345	0.562	4.038	0.685	3.4

without the presence of magnetic field density. The figure shows that the development of magnetic flux density on surface roughness is negligible. A possible explanation might be that in the case of a seamless tube, high peaks are absent in the initial sample, and the abrasive process has removed upper layers from the surface. However, the presence of magnetic flux density shows a significant effect in terms of material removal Fig. 6(*d*). Adding a magnetic field increases the amount of material removed during the process as the pressure of abrasives on the workpiece rises significantly in the presence of magnetic flux. In the case of polishing using non-magnetic slurry, finishing is incomplete, and the finished surface shows more distinctive scratch marks in the circumferential direction, which are visible at higher magnification. The surface polished in the fact of a magnetic field shows complete removal of initial cracks present in the original material and the regular nature of tool marks in the circumferential direction.

The maximum material removal is obtained in the case of 50% abrasive concentration for both IMPs and composite abrasives. This is because, at 50% concentration, the chances of abrasive abrade the surface are maximum. As more abrasive is added to the slurry at a higher concentration, it becomes harder to move the slurry, decreasing overall interaction between abrasive and workpiece, resulting in less material removal.

The results obtained from the SEM imaging of the original surface, the surface finished with the composite abrasives, and the surface finished with the IMPs, both at 50% concentration, are used to assess the morphology of the finished surface.

7.3 Analysis of Original Surface. The workpiece used in the study is a seamless tube of SS316 with artificial scratches created by the wire electro discharge machining (EDM) process. The surface
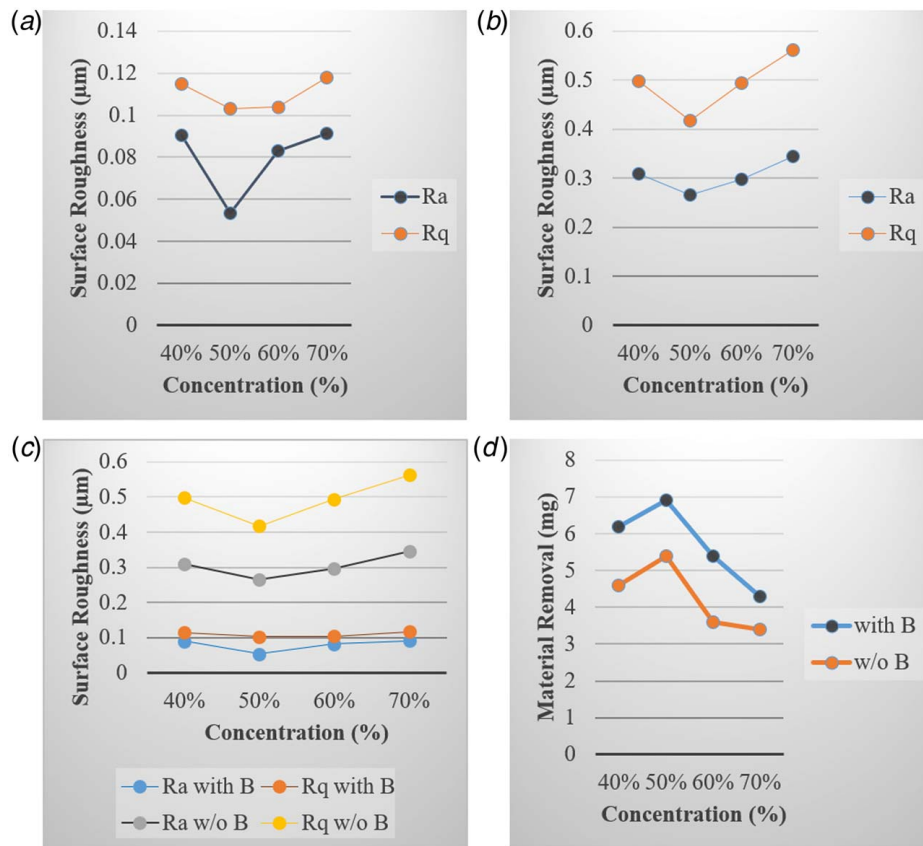
Fig. 6 Surface roughness versus concentration graph: (*a*) in the presence of magnetic flux (*B*) density, (*b*) without magnetic flux density, (*c*) effect of magnetic flux density on surface roughness, and (*d*) material removal graph with varying abrasive concentration
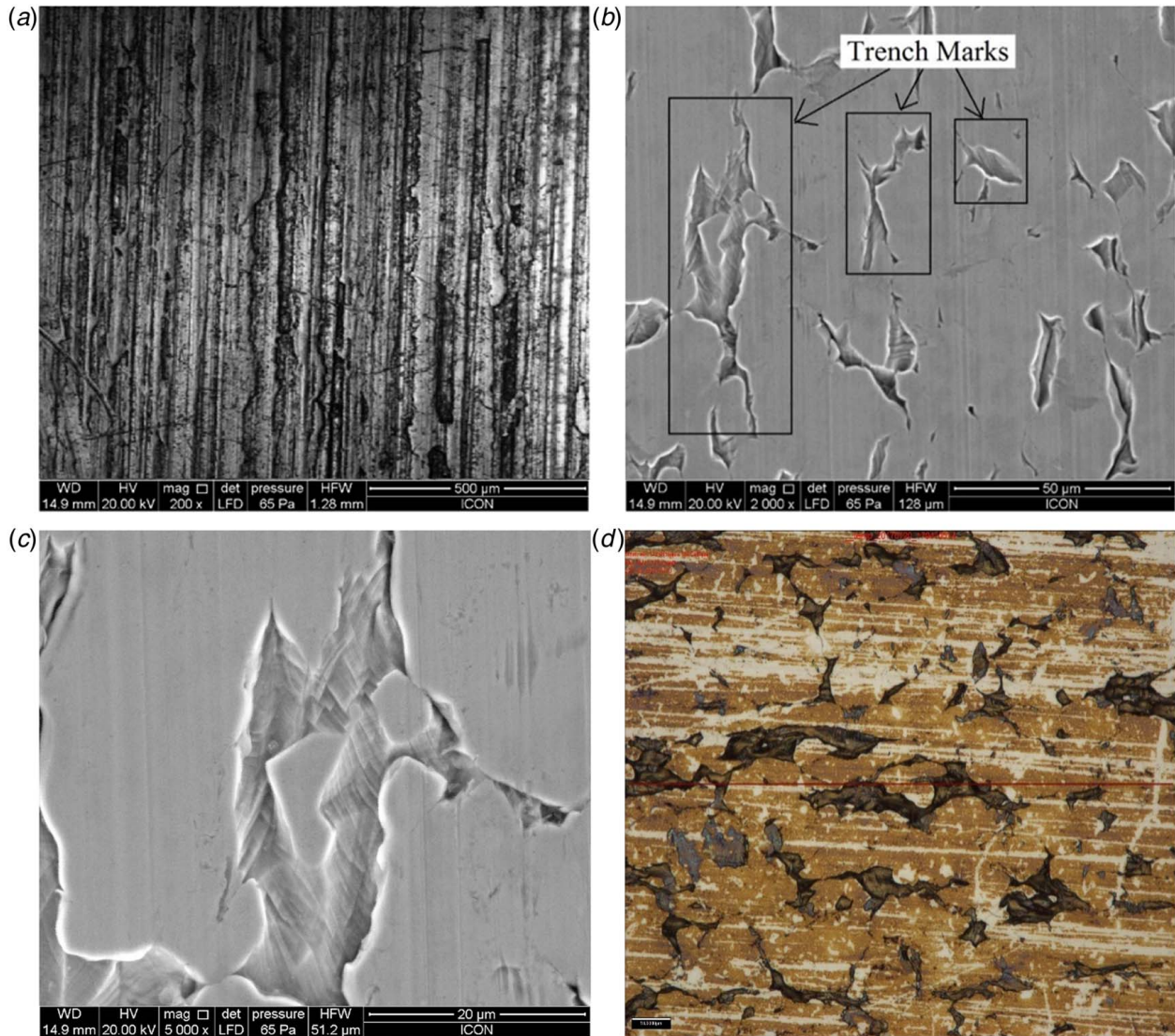
Fig. 7 (a) SEM micro graph of original surface (magnification, 200×; image width of 1.28 mm), (b) magnification 2000× image width 128 μm, (c) magnification, 5000×; image width of 51.2 μm, and (d) surface texture of original surface in axial direction

of a seamless pipe shows the presence of many surface cracks in the axial direction, as shown in Fig. 7. These surface cracks resemble trenches in nature. The width of the crack (in the circumferential direction) is less than its length in the axial direction, and these cracks are deep. Figures 7(c) and 7(d) give a micro-image of the original surface along with the surface texture; it can be observed that the overall surface is smooth and has a minor irregularity compared to the surface crack, whose area is small but poses a higher depth.

7.4 Analysis of the Finished Surface With Composite Abrasive. In the absence of a magnetic field, IMPs were used for finishing. As shown in Fig. 8, the surface of the composite abrasives offers sharp tips of embedded abrasives. Besides that, extrusion marks are not eliminated from the original surface. Non-removal of surface cracks and extrusion die marks from the initial surface show the incomplete finishing. The possible explanation for irregular tool marks can be that heavy intermixing of composite abrasives into the slurry in the presence of a drill-bit and medium self-deformability results in the random motion of composite abrasives. The irregular scratches may be due to the sharp abrasive edges on the composite surface. The presence of scratch marks and abrasive marks represents an irregular nature of finishing by composite

abrasives. The surface finishes without magnetic because the slurry consisting of the composite abrasives is squeezed into the machining gap. Hence, only the squeezing pressure of the composite abrasives is in charge of the material removal mechanism and finish obtained. Experiments reveal that there will be negligible material removal and minor changes in the surface roughness if the slurry concentration is deficient. Hence, finishing in the absence of magnetic flux, it is highly essential to adequately decide the size of the drill-bit and the machining gap.

7.5 Analysis of the Finished Surface With Magneto-Elastic Abrasive. Table 3 shows a complete comparison of the surfaces finished with and without the magnetic field. Magneto-elastic abrasives were used to spend in the presence of a magnetic field. The finished surface shows the complete removal of the upper layer, all the surface cracks present in the original surface are removed, and the finished surface is stable, as shown in Fig. 9. At higher magnification, finishing marks are shown in Figs. 9(b) and 9(c). These finishing marks are regular, and the possible reason for it is shown in Fig. 9(c); in contrast to distinctive patterns observed in Fig. 9(c) can be that on the application of a magnetic field, the abrasives may have formed a chain along magnetic lines of force, thus binding abrasives to each other and preventing random motion of abrasive near the finished surface
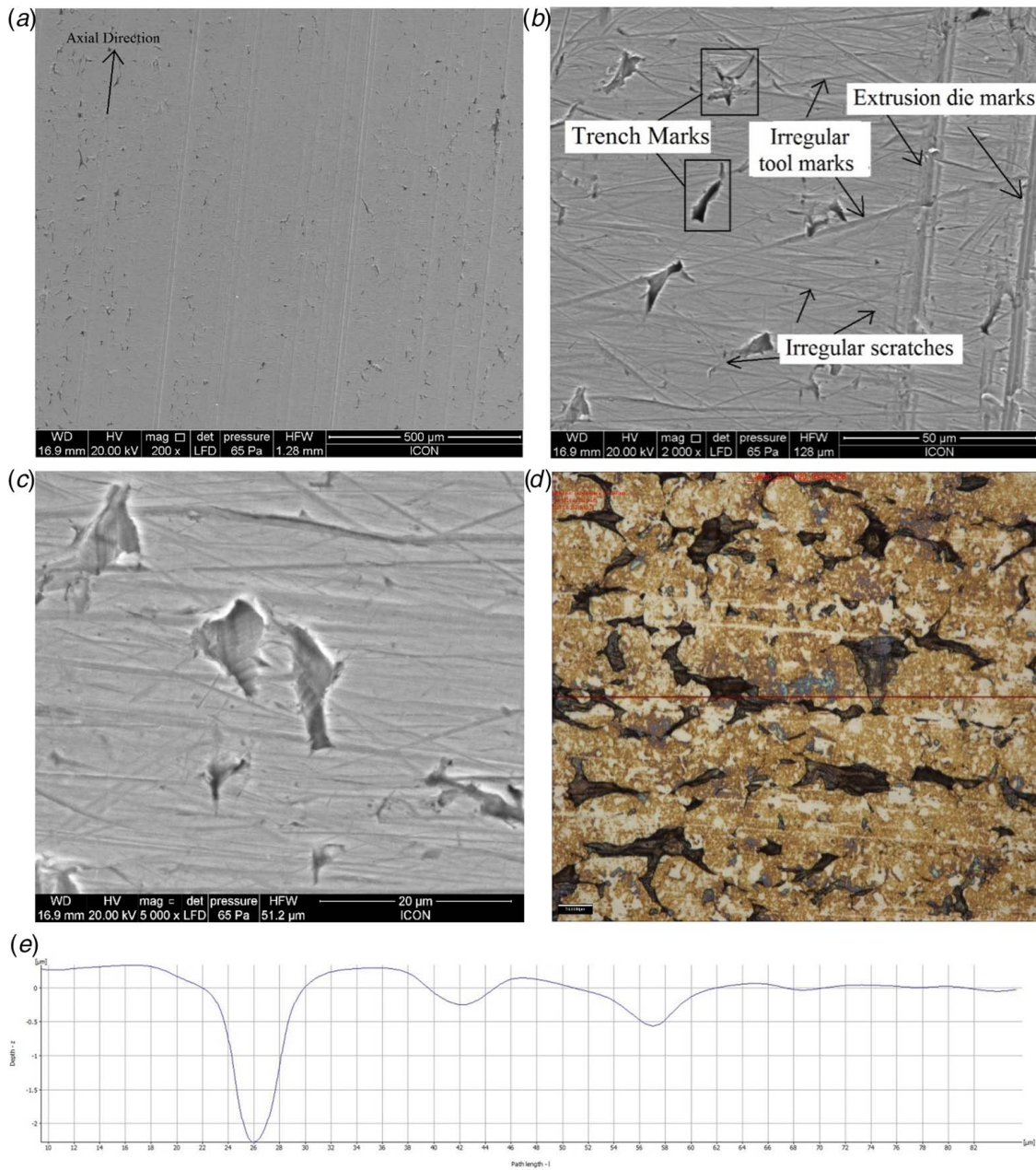
Fig. 8 *(a)* **SEM image of the finished surface with composite abrasive at 50% concentration with** $R_a = 0.266\,\mu m$ **(magnification 200×; image width, 1.28 mm),** *(b)* **magnification of 2000×, image width of 128 μm,** *(c)* $R_q = 0.417\,\mu m$ **(magnification, 5000×; image width of 51.2 μm),** *(d)* **surface texture of finished surface with composite abrasive at 50% concentration in the axial direction, and** *(e)* **profile of the surface under observation**

Table 3 Comparative analysis of the finished surface in the presence and absence of the magnetic field

With magnetic field	Without magnetic field
Averagely 97.54% improvement in roughness average (R_a) of the finished surface was observed concerning the original surface	Averagely 90.59% improvement in the roughness average (R_a) of the finished surface was observed concerning the original surface.
Root mean square (RMS) roughness (R_q) of the finished surface improved averagely 98.18% compared to the original unfinished surface	Root mean square (RMS) roughness (R_q) of the finished surface improved averagely 91.83% compared to the original unfinished surface
As the slurry concentration of IMPs increased, the material removal increased at up to 50% concentration, and then further on, it decreased steadily. The steady decrement was possible as the magnetic force played a vital role in the removal of material removal	The material removal increased to 50% concentration but dropped rapidly beyond 50% of the concentration of the IMPs in the slurry due to no alternate force available for material removal
The best surface finish and material removal possible was at 50% concentration of the slurry, which showcased 98.34% improvement in the R_a concerning the original surface. While the material removal was 6.9 milligram	The best surface finish and material removal were showcased at 50% concentration. Still, it is observed that even at other concentrations, there is no significant difference in the finish and material removal. All the surface roughness and material removal values lie in a close range
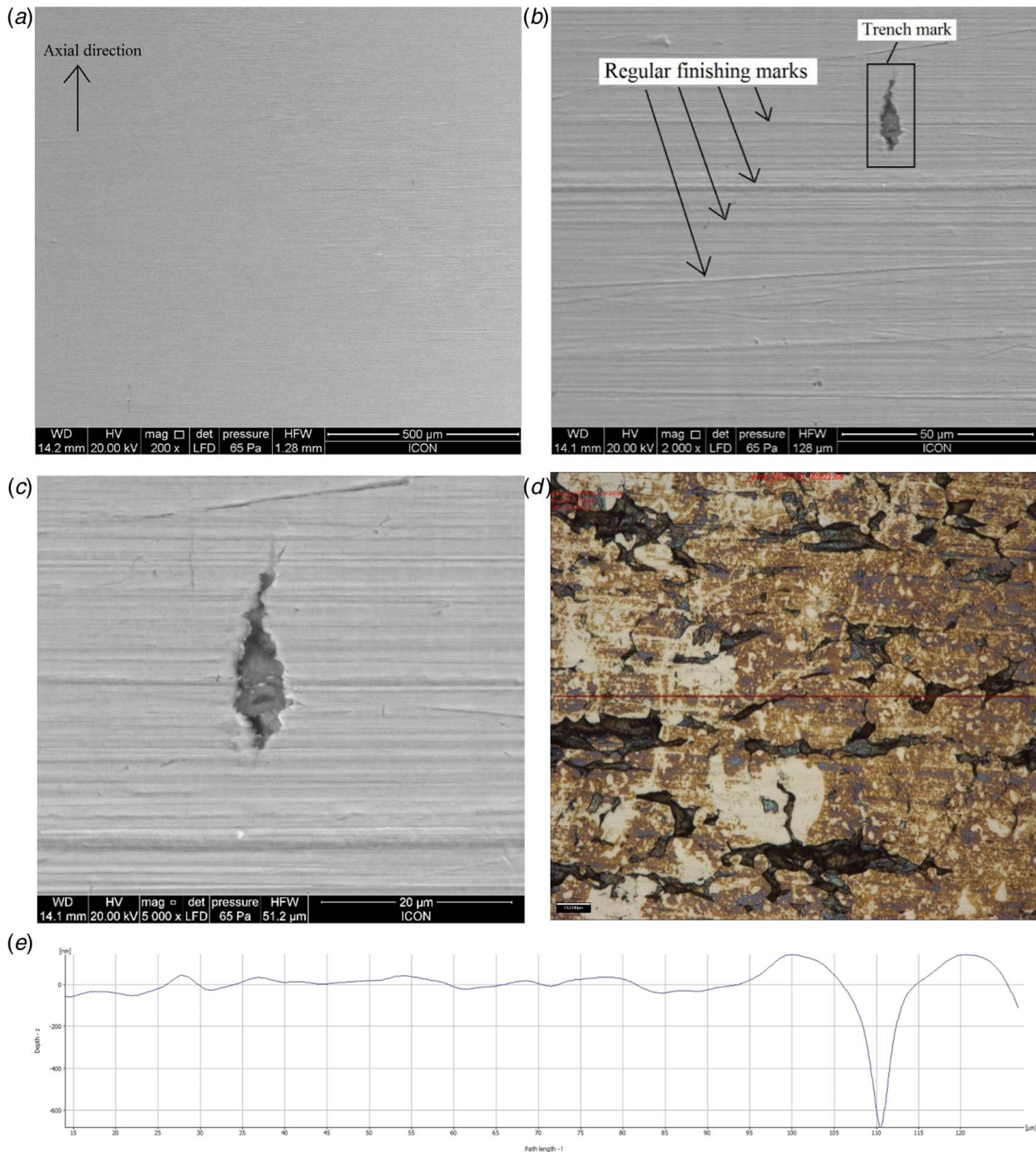
Fig. 9 SEM image of surface finished with magneto-elastic abrasive at 50% concentration: (a) with $R_a = 0.0535 \, \mu$m; magnification of 500×, image width of 512 μm, (b) magnification of 2000×, image width of 128 μm, (c) $R_q = 0.103 \, \mu$m (magnification, 5000×; image width, 51.2 μm), (d) surface texture of finished surface with magneto-elastic abrasive at 50% concentration in the axial direction, and (e) profile of the surface under observation

where the intermixing turbulence is decreased due to viscous drag acting on the particle moving towards the surface.

8 Conclusions

The study completed the development of an EAMSF setup using IMP.

- The minimum surface roughness of $R_a = 0.266 \, \mu$m, $R_z = 3.029 \, \mu$m, and $R_q = 0.417 \, \mu$m was achieved in the absence of the magnetic field at a 50% concentration of IMPs.

- The minimum surface roughness of $R_a = 0.0535 \, \mu$m, $R_z = 0.827 \, \mu$m, and $R_q = 0.103 \, \mu$m was achieved in the presence of the magnetic field at a 50% concentration of IMP. The roughness value Ra = 0.0535 μm is essential while superfinishing of stents.

- The pits in the surface were eliminated only when the process was performed in the presence of a magnetic field, which led to an 82% improvement in the mean peak to valley height (R_z) roughness value of the finished surface.

- The pits did not conform to the actual surface, as the material removal from the overall surface was insignificant in the

absence of a magnetic field. Hence, a mere 6.1% improvement in the mean peak to valley height (R_z) value of surface roughness was observed.

- Maximum material removal detected without a magnetic field is 5.4 mg.
- Maximum material removal detected in the magnetic field is 6.9 mg. Material removal increases by 27% on the 18 mT magnetic field application.
- This indigenously developed method of superfinishing presents promising results in surface roughness and material removal. This method can be widely applied in various precision manufacturing applications such as manufacturing bio-medical appliances like stents, lenses, slip gauges, and measuring instruments.
- The error percentage of the mathematical model is calculated to averagely 1.04% for all readings above 50% concentration, whereas the error is as small as 0.903% for concentrations from 50% to 65%; however, this model is not valid for concentrations below 50% of the concentration of the slurry as all tracks are not accommodated with the impregnated abrasive particles.

Conflict of Interest

There are no conflicts of interest.

Data Availability Statement

No data, models, or code were generated or used for this paper.

References

[1] Jain, V., 2008, "Abrasive-Based Nano-Finishing Techniques: An Overview," Mach. Sci. Technol., **12**(3), pp. 257–294.

[2] Yan, B.-H., Tzeng, H.-J., Huang, F.-Y., Lin, Y.-C., and Chow, H.-M., 2007, "Finishing Effects of Spiral Polishing Method on Micro Lapping Surface," Int. J. Mach. Tools Manuf., **47**(6), pp. 920–926.

[3] Fong, H., and Reneker, D. H., 1999, "Elastomeric Nanofibers of Styrene-Butadiene-Styrene Triblock Copolymer," J. Polym. Sci. B: Polym. Phys., **37**(24), pp. 3488–3493.

[4] Updike, D. P., and Kalnins, A. A., 1972, "Contact Pressure Between an Elastic Spherical Shell and a Rigid Plate," ASME J. Appl. Mech., **39**(4), pp. 1110–1114.

[5] Tian, Y. B., Zhong, Z. W., Lai, S. T., and Ang, Y. J., 2013, "Development of Fixed Abrasive Chemical Mechanical Polishing Process for Glass Disk Substrates," Int. J. Adv. Manuf. Technol., **68**(5–8), pp. 993–1000.

[6] Wani, A. M., Yadava, V., and Khatri, A., 2007, "Simulation for the Prediction of Surface Roughness in Magnetic Abrasive Flow Finishing (MAFF)," J. Mater. Process. Technol., **190**(1–3), pp. 282–290.

[7] Sankar, M. R., Mondal, S., Ramkumar, J., et al., 2009, "Experimental Investigations and Modeling of Drill Bit-Guided Abrasive Flow Finishing (DBG-AFF) Process," Int. J. Adv. Manuf. Technol., **42**(7–8), pp. 678–688.

[8] Sankar, M. R., Jain, V. K., and Ramkumar, J., 2009, "Experimental Investigations Into Rotating Workpiece Abrasive Flow Finishing," Wear, **267**(1–4), pp. 43–51.

[9] Singh, S., and Shan, H. S., 2002, "Development of Magneto Abrasive Flow Machining Process," Int. J. Mach. Tools Manuf., **42**(8), pp. 953–959.

[10] Walia, R. S., Shan, H. S., and Kumar, P., 2009, "Enhancing AFM Process Productivity Through Improved Fixturing," Int. J. Adv. Manuf. Technol., **44**(7–8), pp. 700–709.

[11] Gaikhe, Y. S., Chavan, A. M., and Pawade, R. S., 2013, "Surface Topography Analysis in Electrophoretic Deposition-Assisted Polishing of AISI 316L Stainless Steel," Mater. Manuf. Process., **28**, pp. 676–682.

[12] Jayswal, S., Jain, V., and Dixit, P., 2005, "Modeling and Simulation of Magnetic Abrasive Finishing Process," Int. J. Adv. Manuf. Technol., **26**(5–6), pp. 477–490.

[13] Yuan, Q., Qi, H., and Wen, D., 2016, "Numerical and Experimental Study on the Spiral-Rotating Abrasive Flow in Polishing of the Internal Surface of 6061 Aluminium Alloy Cylinder," Powder Technol., **302**, pp. 153–159.

[14] Saraf, A. R., and Yadav, S. P., 2018," 2—Fundamentals of Bare-Metal Stents, In Functionalised Cardiovascular Stents, J Gerard Wall, H Podbielska, and M Wawrzyńska, eds., Woodhead Publishing, Kidlington, UK, pp. 27–44.

[15] Khalaj Amnieh, S., Mosaddegh, P., and Fadaei Tehrani, A., 2017, "Study on Magnetic Abrasive Finishing of Spiral Grooves Inside of Aluminum Cylinders," Int. J. Adv. Manuf. Technol., **91**(5–8), pp. 2885–2894.

[16] Jain, V. K., 2013, Micromanufacturing Processes, CRC (Taylor and Francis Group), Boca Raton, FL.

[17] Saraf, A. R., Yadav, S. P., and Sadaiah, M., 2018, "Precision Photochemical Machining," Micro and Precision Manufacturing, K Gupta, ed., Springer, Cham, pp. 41–70.

[18] Liao, H. T., Shie, J. R., and Yang, Y. K., 2008, "Applications of Taguchi and Design of Experiments Methods in Optimization of Chemical Mechanical Polishing Process Parameters," Int. J. Adv. Manuf. Technol., **38**(7–8), pp. 674–682.

[19] Kenda, J., Duhovnik, J., Tavčar, J., et al., 2014, "Abrasive Flow Machining Applied to Plastic Gear Matrix Polishing," Int. J. Adv. Manuf. Technol., **71**(1–4), pp. 141–151.

[20] Tian, Y. B., Zhong, Z. W., Lai, S. T., and Ang, Y. J., 2013, "Development of Fixed Abrasive Chemical Mechanical Polishing Process for Glass Disk Substrates," Int. J. Adv. Manuf. Technol., **68**(5–8), pp. 993–1000.

[21] Mali, H. S., and Manna, A., 2012, "Simulation of Surface Generated During Abrasive Flow Finishing of Al/SiCp-MMC Using Neural Networks," Int. J. Adv. Manuf. Technol., **61**(9–12), pp. 1263–1268.

[22] Walia, R. S., Shan, H. S., and Kumar, P., 2006, "Parametric Optimization of Centrifugal Force Assisted Abrasive Flow Machining (CFAAFM) by the Taguchi Method," J. Mater. Manuf. Process., **21**(4–5), pp. 375–382.

[23] Walia, R. S., Shan, H. S., and Kumar, P., 2009, "Enhancing AFM Process Productivity Through Improved Fixturing," Int. J. Adv. Manuf. Technol., **44**(7–8), pp. 700–709.

[24] Kar, K. K., Ravikumar, N. L., Tailon, P. B., Ramkumar, J., and Sathiyamoorthy, D., 2009, "Performance Evaluation and Rheological Characterization of Newly Developed Butyl Rubber Based Media for Abrasive Flow Machining Process," J. Mater. Process. Technol., **209**, pp. 2212–2221.

[25] Jha, S., and Jain, V. K., 2004, "Design and Development of the Magneto Rheological Abrasive Flow Finishing (MRAFF) Process," Int. J. Mach. Tools Manuf., **44**(10), pp. 1019–1029.

[26] Jain, V. K., 2009, "Magnetic Field Assisted Abrasive Based Micro-/Nano-Finishing," J. Mater. Process. Technol., **209**(20), pp. 6022–6038.

[27] Das, M., Jain, V. K., and Ghoshdastidar, P. S., 2012, "Nanofinishing of Flat Workpieces Using Rotational–Magnetorheological Abrasive Flow Finishing (R-MRAFF) Process," Int. J. Adv. Manuf. Technol., **62**(1–4), pp. 405–420.

[28] Chen, W.-C., Wu, K.-L., and Yan, B.-H., 2014, "A Study on the Application of Newly Developed Magneto-Elastic Abrasive to Improving the Surface Roughness of the Bore," Int. J. Adv. Manuf. Technol., **73**(9–12), pp. 1557–1566.

[29] Ravi Sankar, M., Jain, V. K., and Ramkumar, J., 2010, "Rotational Abrasive Flow Finishing (R-AFF) Process and Its Effects on Finished Surface Topography," Int. J. Mach. Tools Manuf., **50**(7), pp. 637–650.

[30] Yadav, S. P., Waikar, R., Pawade, R. S., and Joshi, S. S., 2017, "Experimental Analysis of Orthogonal Micro-Machined Surface Features and Chip Morphology of AISI1215 Steel by Using EBSD Method," Proceedings of the International Conference on Communication and Signal Processing 2016 (ICCASP 2016), Raigad, India, Dec. 20–21, pp. 304–310.

[31] Stradling, A. W., 1993, "The Physics of Open-Gradient Dry Magnetic Separation," Int. J. Miner. Process., **39**(1–2), pp. 1–18.

[32] Kutzelnigg, W., Fleischer, U., and Schindler, M., 1990, "The IGLO-Method: Ab-Initio Calculation and Interpretation of NMR Chemical Shifts and Magnetic Susceptibilities," Deuterium and Shift Calculation, 23, ed., Springer, Berlin, Heidelberg.

[33] Rabinowicz, E., Dunn, L. A., and Russel, P. G., 1961, "A Study of Abrasive Wear Under Three-Body Conditions," Wear, **4**(5), pp. 345–355.

[34] Yadav, S. P., Saraf, A. R., and Sadaiah, M., 2017, "Analysis of Undercut for SS304 in Photochemical Machining," Proceedings of the International Conference on Communication and Signal Processing 2016 (ICCASP 2016), Raigad, Dec. 20–21, pp. 284–289.

[35] Saraf, A. R., and Sadaiah, M., 2017, "Photochemical Machining of a Novel Cardiovascular Stent," Mater. Manuf. Processes, **32**(15), pp. 1740–1746.

[36] Jefimenko, O. D., 1966, Electricity and Magnetism, Meredith Publishing Company, New York.

[37] Zohdi, T. I., 2015, "An Introduction to the Finite-Element Method," Mechanical Engineers' Handbook, pp. 1–22.

[38] Sukumar, N., and Bolander, J. E., 2003, "Numerical Computation of Discrete Differential Operators on Non-Uniform Grids," Comput. Model. Eng. Sci, **4**(6), pp. 691–706.

[39] María Jesús, M. G., Raúl, I. M., Emilio, G. R., and Carlos, D. M., 2011, "Complex Polar Coordinates in Electromagnetics," J. Electromagn. Waves Appl., **25**(2–3), pp. 389–398.